

Interactions between aerosol absorption, thermodynamics, dynamics, and microphysics and their impacts on a multiple-cloud system

Seoung Soo Lee¹  · Zhanqing Li¹ · Jungbin Mok¹ · Myoung-Hwan Ahn² · Byung-Gon Kim³ · Yong-Sang Choi⁴ · Chang-Hoon Jung⁵ · Hye Lim Yoo⁶

Received: 4 June 2016 / Accepted: 24 January 2017 / Published online: 17 February 2017
© Springer-Verlag Berlin Heidelberg 2017

Abstract This study investigates how the increasing concentration of black carbon aerosols, which act as radiation absorbers as well as agents for the cloud-particle nucleation, affects stability, dynamics and microphysics in a multiple-cloud system using simulations. Simulations show that despite increases in stability due to increasing concentrations of black carbon aerosols, there are increases in the averaged updraft mass fluxes (over the whole simulation domain and period). This is because aerosol-enhanced evaporative cooling intensifies convergence near the surface. This increase in the intensity of convergence induces an increase in the frequency of updrafts with the low range of speeds, leading to the increase in the averaged updraft mass fluxes. The increase in the frequency of updrafts induces that in the number of condensation entities and this leads to more condensation and cloud liquid that acts to be a source of the accretion of cloud liquid by precipitation. Hence, eventually, there is more accretion that offsets

suppressed autoconversion, which results in negligible changes in cumulative precipitation as aerosol concentrations increase. The increase in the frequency of updrafts with the low range of speeds alters the cloud-system organization (represented by cloud-depth spatiotemporal distributions and cloud-cell population) by supporting more low-depth clouds. The altered organization in turn alters precipitation spatiotemporal distributions by generating more weak precipitation events. Aerosol-induced reduction in solar radiation that reaches the surface induces more occurrences of small-value surface heat fluxes, which in turn supports the more low-depth clouds and weak precipitation together with the greater occurrence of low-speed updrafts.

Keywords Aerosol · Mesoscale convective system · Evaporation · Stability · Gust front

✉ Seoung Soo Lee
cumulss@gmail.com; slee1247@umd.edu

¹ Earth System Science Interdisciplinary Center, University of Maryland, College park, MD, USA

² Department of Atmospheric Science and Engineering, Ewha Womans University, Seoul, South Korea

³ Department of Atmospheric Environmental Sciences, Gangneung-Wonju National University, Gangneung, Gang-Won do, South Korea

⁴ Department of Environmental Science and Engineering, Ewha Womans University, Seoul, South Korea

⁵ Department of Health Management, Kyungin Women's University, Incheon, South Korea

⁶ Earth Resources Technology, Inc., National Oceanic and Atmospheric Administration, College Park, MD, USA

1 Introduction

Black carbon (BC) aerosols (or absorbing aerosols) have been known to modify the temperature profile of the atmosphere by absorbing solar radiation. This modification raises the temperature of the atmosphere and lowers the level of solar radiation that reaches the surface and thus of temperature, latent and sensible heat fluxes at the surface (Segal and Arritt 1992; Jacobson 2006, 2012; Ten Hoeve et al. 2012).

Considering the important roles played by stability and surface fluxes on clouds and precipitation (e.g., Houze 1993; Lee et al. 2008a, 2014a), the probable BC-aerosol-induced changes in stability and surface fluxes may alter the development of clouds, their associated microphysics, and precipitation. Moreover, the BC-aerosol-induced

heating of the atmosphere and cooling at the surface have been shown to interact with cloud dynamical fields (e.g., updrafts) at various scales, thus altering cloud processes (Ramanathan et al. 2001; Lau et al. 2008; Wang 2009; Lee et al. 2014a). Although changes in atmospheric radiative heating, surface cooling, and associated changes in surface heat fluxes, microphysics, and precipitation induced by increases in BC-aerosol loading have been extensively observed and discussed, their interplay with cloud dynamics has not yet been clearly understood (Tao et al. 2012).

In multiple-cloud systems, interactions among cloud cells create interesting features such as self-organization (or cloud-system organization) of the systems (Baker and Charlson 1990; Heylighen 2002; Morrison et al. 2012). Self-organization is defined as a system-wide pattern that arises from interactions among cloud cells. The organization can be characterized by the spatiotemporal variability of cloud properties such as cloud-cell depths and population (Lee and Feingold 2013; Lee et al. 2014b). Few studies have investigated BC-aerosol-induced changes in stability, surface fluxes, microphysics, precipitation and dynamics in the context of cloud systems and their organization. Note that the organization is ultimately closely linked to precipitation spatiotemporal distributions or how precipitation with different intensities is distributed in time and space (Storer et al. 2010; Lee 2011a; Lee and Feingold 2013). Hence, it is needed to not only improve our understanding of interactions between BC-aerosol loading, stability, surface fluxes, microphysics, precipitation and dynamics, but also to examine their interactions in terms of cloud-system properties such as cloud-system organization. Toward this goal, this study investigates these interactions and their association with cloud-system organization and precipitation distributions.

To fulfill the goal, numerical simulations are performed using a cloud-system resolving model (CSRМ) that resolves cloud cells and cloud processes. Using the CSRМ, a mesoscale convective system (MCS) or a mesoscale cloud ensemble (MCE) is simulated. The MCS here is composed of various types of clouds from deep convective clouds whose tops grow to reach the tropopause to warm clouds whose tops are below the freezing level through shallow mixed-phase convective clouds whose tops are below the tropopause but above the freezing level. First, in the simulated MCS, we examine how increasing BC-aerosol loading affects total precipitation amount as traditionally examined in the previous studies (e.g., Rosenfeld 1999; Andreae et al. 2004; Qian et al. 2009; Wang 2013). Then, we identify associated cloud microphysical and dynamic processes in the context of aerosol-induced changes in stability. To better understand mechanisms that control aerosol effects on precipitation amount and associated cloud processes, we

also perform analyses on cloud-system organization, precipitation distributions and surface fluxes.

2 The CSRМ

The Advanced Research Weather Research and Forecasting (ARW) model, a non-hydrostatic compressible model, is the CSRМ selected for use in this study. A fifth-order monotonic advection scheme is used for the advection of cloud variables (Wang et al. 2009). Simulations consider radiation processes by adopting the Rapid Radiation Transfer Model (RRTMG) (Fouquart and Bonnel 1980; Mlawer et al. 1997).

The model in this study uses the bulk double-moment microphysics parameterization that emulates the bin microphysics scheme for the calculation of collection and sedimentation processes. This parameterization is generally referred to as a bin-bulk scheme and has been first implemented into Regional Atmospheric Modeling System (RAMS) at Colorado State University. This bin-bulk scheme has been created by Walko et al. (1995) and Meyers et al. (1997) and further developed by Saleeby and Cotton (2004, 2008). This study adopts the version of the bin-bulk scheme that is developed by Saleeby and Cotton (2004, 2008). For this study, nucleation parameterizations in this version of the scheme are replaced by those that are described in Lee et al. (2010). The size distribution of hydrometeors in the double-moment scheme used here obeys a generalized gamma distribution with fixed breadth. There are seven classes of hydrometeors in the double-moment scheme used here: droplets, rain, pristine ice, snow, aggregates, hail, and graupel. More details about the double-moment scheme used in this study are found in Lee et al. (2010) and Saleeby and Cotton (2004, 2008).

In this study, the radiative effect of aerosols is considered. It is assumed that aerosol particles are internally composed of 6% BC and 94% organic compound by mass based on observations made by Allen et al. (2008). Aerosol particles also act as cloud condensation nuclei (CCN) and ice nuclei (IN). Based on this assumed mixture, the associated densities, and the ambient relative humidity, the radiative and activation characteristics of aerosol particles are calculated. For example, single scattering albedo is approximately 0.89 at a wavelength of 470 nm for dry aerosol particles.

The aerosol mass mixing ratio is transported and removed from the atmosphere by nucleation and impacting scavenging. The supersaturation of air parcels is predicted and the predicted supersaturation is used for the activation of aerosol particles. Activated aerosol particles or mass is carried among hydrometeors by collision-coalescence and removed from the atmosphere once hydrometeors that

contain aerosols reach the surface. Following Feingold and Kreidenweis (2002), we assume that when a portion of the total hydrometeor mass of an original (hydrometeor) class is transported to a different class by microphysical processes such as collision-coalescence, the ratio of the aerosol mass (to the total aerosol mass) that is transported from the original class (in which the total aerosol mass is embedded before the transportation) to the different class is the same as the ratio of the hydrometeor mass (to the total hydrometeor mass before the transportation) of the original class that is transported. Aerosols return to the atmosphere upon evaporation or sublimation of hydrometeors that contain aerosols.

3 Case description and simulations

The Tropical Warm Pool - International Cloud Experiment (TWP-ICE, 06:00 Local Solar Time (LST) January 23rd to 12:00 LST January 25th 2006) is carried out in Darwin, Australia (12.42°S, 130.89°E) (Fridlind et al. 2010, 2012; Zhu et al. 2012) and an MCE is observed during the TWP-ICE campaign. This MCE involves deep convective clouds reaching the tropopause and interacting with mixed-phase and warm clouds, as depicted by Zhu et al. (2012). A simulation of this MCE over the TWP-ICE period of 2 days and 6 h is performed over a three-dimensional domain and this simulation is referred to as the control run.

Large-scale forcings that represent synoptic-scale environment are imposed on the control run at each time step by performing the temporal interpolation of the three-hourly observed soundings and the calculation of the tendencies of potential temperature and specific humidity based on the interpolated soundings (e.g., Fridlind et al. 2010, 2012). For all simulations in this study, identical large-scale forcings are applied. Hence, the identical advection, convergence and divergence of temperature and humidity at synoptic scales are applied to all simulations in this study.

The TWP-ICE observation site includes both land and ocean areas (Fridlind et al. 2010, 2012). The low-lying land areas in the TWP-ICE domain become saturated during the monsoon season and behave in a manner that has been characterized as maritime in nature. Based on this and following Fridlind et al. (2010, 2012), the ocean surface type in the control run is assumed. Land areas that have been characterized as maritime in nature enable comparisons between the control run over the ocean surface and observation over the TWP-ICE site. Surface heat fluxes and sea surface temperature are predicted by the Noah land surface model (LSM) (Chen and Dudhia 2001).

A MCS (or MCE) is defined as a system which has its spatial length of ~ 100 km or more in any direction (Houze 1993). Based on this definition, 120 km is adopted as the

length of the horizontal domain, while 20 km is applied to the length of the vertical domain to simulate the mesoscale system for the control run. Moreover, this domain length for the control run is similar to that of the TWP-ICE observation domain. Fridlind et al. (2010, 2012) suggested that simulations should be performed over a domain whose size is similar to that of the TWP-ICE observation domain, since this enables reasonable comparisons between simulations and observations. The horizontal (vertical) grid spacing is 500 m (200 m). Periodic boundary conditions are applied to simulations.

The initial size distribution and number concentration of background aerosol are shown in Fig. 1. Figure 1 is only for the altitude of 0.5 km in the planetary boundary layer (PBL) where aerosol concentration is higher than in other layers and it is assumed that the size distribution follows a tri-modal log-normal distribution. Modal diameter and distribution breadth of each of modes of the size distribution are assumed not to vary spatiotemporally, hence, aerosol particles in any grid points have the shape of the size distribution in Fig. 1. Based on the assumed tri-modal log-normal distribution, the predicted aerosol mass is used to diagnose the aerosol number concentration that varies spatiotemporally due to clouds, advection, and diffusion.

The assumption of unchanged size distribution can lead to an overestimate of CCN available for in-cloud nucleation (or secondary nucleation). This deficiency is found to be unimportant for strong convection here, because most of CCN are found to be readily consumed by primary nucleation. The primary nucleation occurring in cloud-free environment predominantly determines cloud droplet number concentration (CDNC) and associated droplet size (i.e., microphysical factors). Hence, the role of the secondary nucleation (occurring in clouds) in microphysical factors, and cloud dynamics and cloud-system organization (i.e., macrophysical factors that are closely linked to microphysical factors) is negligible.

The background aerosol number concentration averaged over the PBL at the first time step in the accumulation

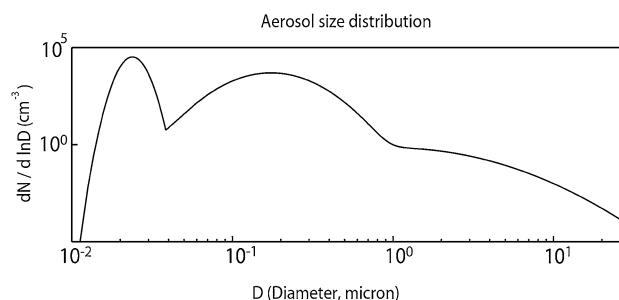


Fig. 1 Aerosol size distribution at an altitude of 0.5 km. N represents the aerosol number concentration per unit volume of air and D represents the aerosol diameter

mode is $\sim 100 \text{ cm}^{-3}$. Note that most of CCN calculated with the general supersaturation range in nature are in accumulation mode. The accumulation-mode vertical distribution of aerosol concentrations at the first time step that is applied to the control run is shown in Fig. 2. This vertical distribution is measured by aerosol counters and probes on the Egret and Dornier aircraft (Vaughan et al. 2008). As mentioned in the introduction, this study focuses on the effect of BC-aerosol loading that contains a specific amount of BC, but not on aerosol chemical composition. So, to examine and isolate the effect of increases in BC-aerosol loading, the control run is repeated using an aerosol number concentration, or loading, at the initial time step that is increased by a factor of 3 in a layer between 1.5 and 3.1 km in altitude but with no changes in aerosol chemical composition. The increase in aerosol loading is based on Allen et al. (2008) who collected numerous cases of BC-aerosol pollution at the TWP-ICE site and made a composite of those cases. The composite showed that the perturbation of aerosols containing BC at and around the site of the TWP-ICE campaign occurred frequently in that layer or in a layer straddling similar altitudes. The composite also showed that the perturbation involves increases in aerosol concentration by a factor of ~ 3 . The repeated simulation is referred to as the

high-aerosol run. The accumulation-mode vertical distribution of aerosol concentrations at the first time step for the high-aerosol run is depicted in Fig. 2.

In addition to the control run and the high-aerosol run, more simulations were performed to support findings in this study. While a detailed description of those simulations is given in the following sections, a brief description is given in Table 1. Note that all the simulations in this study adopt identical model setup (e.g., large-scale forcings and grid length) except for differences among them as described in Table 1 and in the following sections.

4 Results

4.1 Temperature and stability

The vertical distributions of the time- and area-averaged radiative heating for the control run and the high-aerosol run from the start of the simulations to 12:00 LST on January 23rd, which is 5 min before the first cloud cell in the control run forms, is shown in Fig. 3. In this study, to obtain the area-averaged value of a variable of interest at each altitude to construct a figure such as Fig. 3, we collect grid points with non-zero values of the variable at each altitude and each time step. Then, we sum up those values over these grid points with non-zero values at each altitude and each time step. Then, this sum is divided by the number of all grid points in the horizontal domain (whether these grid points have non-zero values or zero values) to obtain the area-averaged value of the variable at each altitude and each time step. In the following analysis, the domain-averaged value (or the value averaged over the domain) means the value averaged over the whole domain throughout all altitudes. For this value, we collect grid points with non-zero values of the variable throughout all altitudes over the whole domain and sum up these values over these grid points with non-zero values at each time step. Then, this sum is divided by the number of all grid points over the whole domain throughout all altitudes (whether these grid points have non-zero values or zero values) to obtain the domain-averaged value of the variable at each time step.

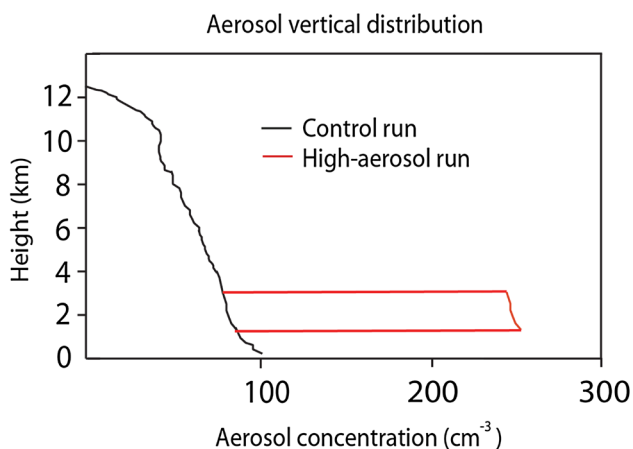


Fig. 2 Vertical distributions of aerosol concentration in the accumulation mode at the first time step for the control run and the high-aerosol run,

Table 1 A description of simulations

Simulations	Aerosol concentration in the layer between 1.5 and 3.1 km	Cooling from cloud-liquid evaporation
Control run	Observed	Considered
High-aerosol run	3 times greater than in the control run	Considered
Control-noevp run	Observed	Not considered
High-aerosol-noevp run	3 times greater than in the control run	Not considered

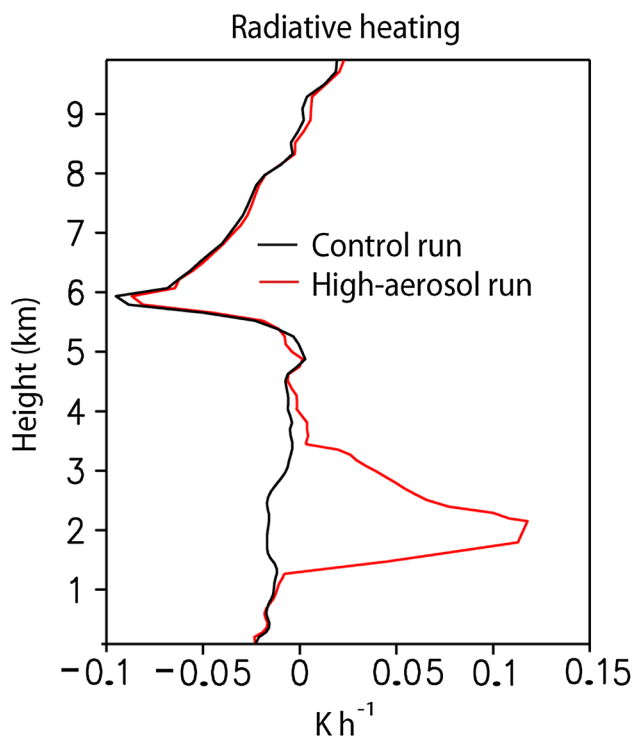


Fig. 3 Vertical distributions of the time- and area-averaged net radiative heating from the beginning of the simulations to 12:00 LST on January 23rd for the control run and the high-aerosol run

In general, the high-aerosol run has larger radiative heating than the control run does due to the larger concentration of solar-radiation-absorbing aerosols (Fig. 3). Most of the differences in the heating between the runs are seen between 1.5 and 3.1 km because a larger concentration of aerosols is imposed in the high-aerosol run for that layer at the initial time step. Associated with the larger radiative heating up until 12:00 LST on January 23rd, the high-aerosol run shows the higher potential temperature than the control run does between ~0.5 and ~4.5 km (Fig. 4). In the layer between ~0.5 and ~4.5 km, the high-aerosol run develops a greater stability than the control run does. This stability acts as an initial condition for the clouds that start to form around 12:00 LST on January 23rd. Due to the higher aerosol-induced radiative heating, the subsequent clouds in the high-aerosol run experience a more stabilized environment than those in the control run. Associated with the more stabilized environment, the first cloud cell forms 10 min later in the high-aerosol run than in the control run. The first cloud cell forms at 12:05 LST and 12:15 LST on January 23rd in the control run and the high-aerosol run, respectively. In the following sections, analyses of results are performed for the period from 12:00 LST on January 23rd to 12:00 LST January 25th.

To grant confidence to results here, first of all, we need to evaluate the simulations and the evaluation is performed

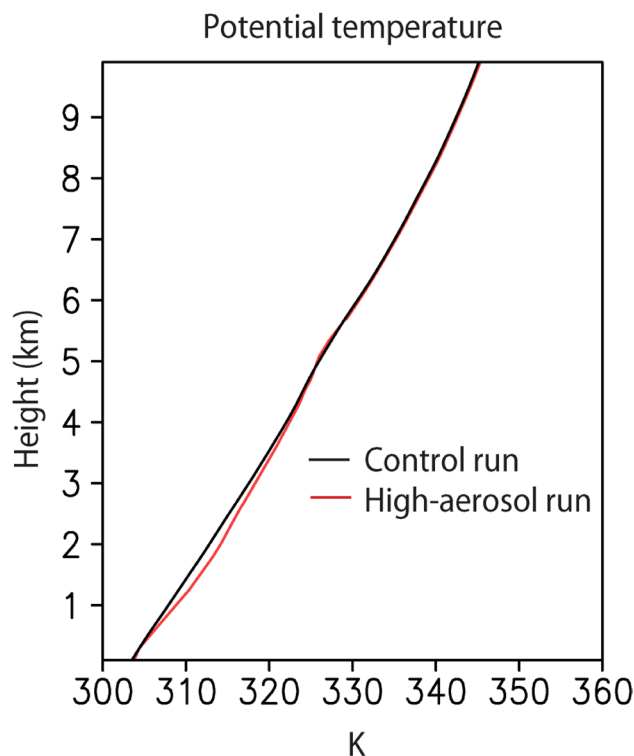


Fig. 4 Vertical distributions of the area-averaged potential temperature in the control run and the high-aerosol run at 12:00 LST on January 23rd

in the following Sect. 4.2. In Sect. 4.2, we also examine aerosol effects on precipitation amount or cumulative precipitation as conventionally done in the previous studies. This examination enables comparisons between this study and the previous studies.

4.2 Microphysics, precipitation and cloud radiative forcing (CRF)

Area-mean rain rates or precipitation rates at the surface smoothed over 3 h for the control run and the high-aerosol run are shown in Fig. 5a. The simulated precipitation rate in the control run follows its observed counterpart well, which demonstrates that the simulations perform reasonably well. Supporting that simulations are performed reasonably well, cloud-top-height and cloud-size frequency distributions show a fairly good agreement between observations and the control run as shown in Fig. 5b, c. By utilizing reflectivity data from Multi-functional Transport Satellites (MTSAT), first, we identify cloud-top height at every observation grid point that corresponds to the simulation grid point and construct the distribution of cloud-top-height frequency. This observed distribution is compared to the simulated counterpart as shown in Fig. 5b. Figure 5b indicates that the control run and observations both have varying classes

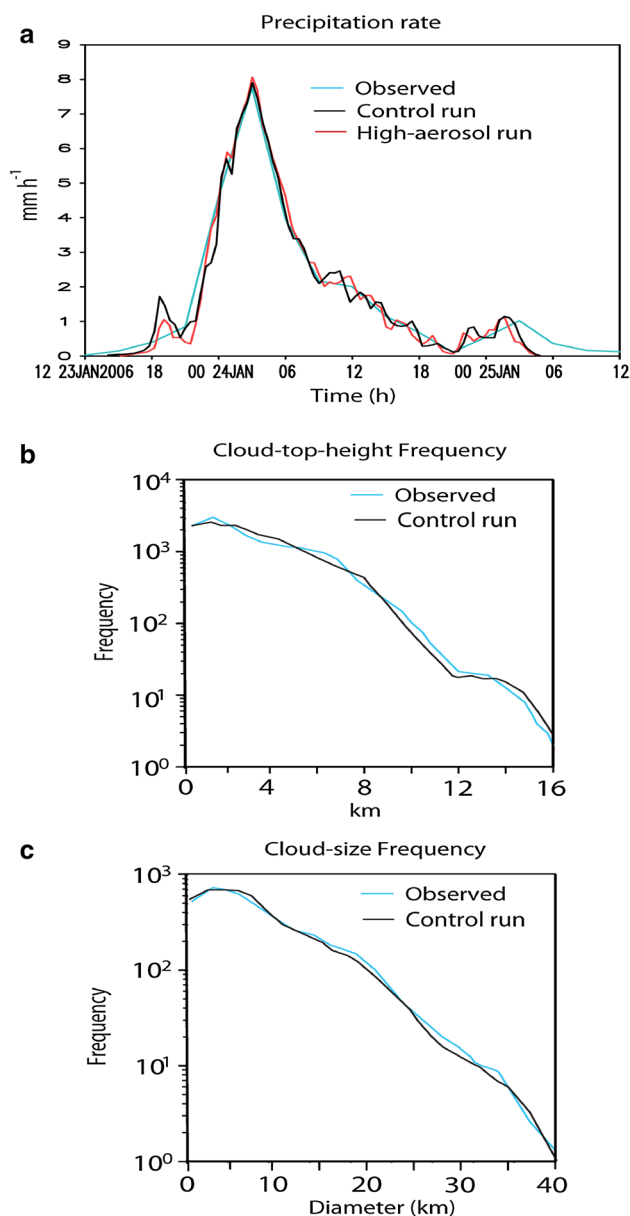


Fig. 5 **a** Time series of the area-averaged precipitation rates in observations, the control run, and the high-aerosol run. Distributions of **b** cloud-top-height frequency and **c** cloud-size frequency (over cloud-cell diameter) in observations and the control run

of clouds: warm clouds whose tops are below the freezing level, mixed-phase clouds whose tops are above the freezing level and below the tropopause and deep convective clouds that grow to the tropopause. The averaged freezing level and the averaged level of the tropopause are 3.5 and 17 km, respectively. Then, we identify cloud cells by looking at cloud optical depth (COD) in the MTSAT observation and the control run. After those cloud cells are identified, an area that a cloud cell occupies is calculated and we transform the area to a circle that has an equal area to

the area which the selected cloud cell occupies. We obtain the diameter of the circle and this diameter is used as the size of the selected cloud cell. This way of obtaining the diameter is repeatedly applied to all identified cloud cells. Finally, we obtain the sizes of all identified clouds and these sizes are used to construct the distributions of the cloud-size frequency in observation and the control run. These distributions in observation and the control run are compared in Fig. 5c.

The control run and the high-aerosol run show the similar time series of the area-averaged precipitation rate and thus the similar cumulative precipitation. The percentage difference in the cumulative precipitation at the last time step is ~3% between the runs; the high-aerosol run has ~3% greater cumulative precipitation. Although precipitation enhancement occurs in the high-aerosol run, the difference in total precipitation seems insignificant despite the three-fold increase in aerosol concentration in the layer between 1.5 and 3.1 km in the high-aerosol run. This is contrary to the previous studies that show much smaller total precipitation amount in polluted cases than in the clean cases (Rosenfeld 1999; Andreae et al. 2004; Qian et al. 2009; Wang 2013). As a first step to understand this, we perform analyses on sources and sinks of precipitation as follows.

The averaged differences in the sources and sinks of hydrometeors between the high-aerosol run and the control run are calculated and shown in Table 2. For the calculation of these differences, the sum of cumulative values of each of these sources and sinks over the whole domain at the last time step is obtained and divided by the area of the horizontal domain for each run; for details of this calculation, see Lee et al. (2008b). These sources and sinks are obtained for the whole mass of hydrometeors that are able to precipitate, following Lee et al. (2008b). As found by Lee et al. (2008a), among the differences in precipitation sources and sinks that are caused by aerosol increases, those in autoconversion and the microphysical processes that are related to accretion (or collection) of cloud liquid are dominant. That is, aerosol-induced increases in accretion of cloud liquid by precipitation (or precipitable hydrometeors) mostly offset aerosol-induced decreases in autoconversion and result in the small difference in the precipitation amount: in this study, rain, snow, graupel, and hail constitute precipitable hydrometeors and for the expediency of budget analyses of precipitable hydrometeors, graupel includes hail in budget analyses here. However, terms associated with cloud ice, particularly accretion of cloud ice by precipitation, have negligible impacts on the differences in precipitation between the runs. This is mainly associated with the very low ice water path (IWP) and its variation with the increase in aerosol concentration compared to the liquid water path (LWP) and its variation. Here, the IWP and the LWP are the vertical integrals of cloud-ice

Table 2 Differences in cumulative sources and sinks of precipitation between the high-aerosol run and the control run, averaged over the study domain

Sources and sinks of precipitation (mm)	Difference (high-aerosol run – control run)
Sources	
Autoconversion	-10.47
Accretion of cloud liquid by rain	9.57
Accretion of cloud liquid by graupel	2.62
Accretion of cloud liquid by snow	0.95
Accretion of cloud liquid by cloud ice	0.39
Accretion of cloud ice by snow	0.03
Accretion of cloud ice by rain	0.01
Hallet-Mossop ice production	0.00
Condensation onto rain	-0.42
Deposition onto cloud ice	0.30
Deposition onto snow	-0.03
Deposition onto graupel	0.42
Freezing of cloud liquid	0.00
Sinks	
Evaporation of rain	-0.21
Sublimation of snow	-0.13
Sublimation of cloud ice	0.38
Sublimation of graupel	0.53
Precipitation	2.80

Table 3 Cumulative cloud-liquid condensation, cloud-liquid evaporation, glaciation, and sublimation, averaged over the study domain

Simulations	Condensation (mm)	Evaporation (mm)	Glaciation (mm)	Sublimation (mm)
Control	181	91	23	15
High-aerosol	252	159	31	22
High-aerosol minus control	71	68	8	7

content and cloud-liquid content over the vertical domain, respectively. The time- and area-averaged IWP is 77 and 85 g m⁻², while the time- and area-averaged LWP is 819 and 980 g m⁻² in the control run and the high-aerosol run, respectively. Hence, there are ~20 times larger increases in cloud-liquid mass (or the LWP) than in cloud-ice mass (or the IWP) with the increase in aerosol concentration. Thus, there are much larger increases in cloud-liquid mass than in cloud-ice mass that can be collected or accreted by precipitable hydrometeors. This leads to much larger increases in accretion of cloud liquid by precipitable hydrometeors than in accretion of cloud ice by precipitable hydrometeors. The much smaller increases in accretion of cloud ice is partly attributed to the fact that the altitudes of cloud ice tend

to higher than those of precipitable hydrometeors, which reduce chances for cloud-ice particles to collide with precipitable hydrometeors.

Table 3 shows that condensation onto cloud liquid and its variation as the aerosol concentration increases are about one order of magnitude larger than glaciation and its variation as the aerosol concentration increases. Here, glaciation comprises all cloud processes that transform none-solid-phase particles to solid-phase particles. Thus, glaciation includes deposition as well as freezing or riming processes.

Considering that condensation and glaciation are main production mechanisms for cloud liquid and solid-phase particles (one class of which is cloud ice), respectively, condensation and its variation shown in Table 3 can reasonably explain why the LWP and its variation are much larger than the IWP and its variation. As discussed in Lee et al. (2008b), this large increase in condensation results in the large increase in cloud liquid or the LWP.

Associated with aerosol-induced increases in the LWP and the IWP, there are aerosol-induced increases in CRF. To calculate CRF, we collect the net shortwave radiation fluxes over grid points at the top of cloudy grid columns where the sum of the LWP and the IWP is not zero. Here, for the calculation of the net fluxes, we assign a plus (minus) sign to upward (downward) fluxes. These net fluxes are summed over those grid points (associated with the cloudy grid columns) and divided by the number of those grid points to obtain the averaged net flux over cloudy grid columns at each time step, referred to as F_{cld} . Then, we collect the net shortwave radiation fluxes over grid points at the top of non-cloudy grid points where the sum of the LWP and the IWP is zero. These net fluxes are summed over those grid points (associated with the non-cloudy grid columns) and divided by the number of those grid points to obtain the averaged net flux over non-cloudy grid columns at each time step, referred to as F_{clr} . " F_{clr} minus F_{cld} " is defined to be CRF at each time step. The time-averaged " F_{clr} minus F_{cld} " over the period we focus on is -108.26 W m^{-2} and -176.45 W m^{-2} in the control run and the high-aerosol run, respectively. Hence, there is an aerosol-induced increase in the negative CRF by 68.19 W m^{-2} . At each time step, cloud albedo, the ratio of upward shortwave radiation fluxes to the absolute value of downward shortwave fluxes, is also obtained over grid points at the top of cloudy grid columns. Then, cloud albedo is averaged over those grid points (associated with the cloudy grid columns) at each time step and the averaged cloud albedo at each time step is averaged again over the period we focus on to obtain the time-averaged cloud albedo. Associated with the increase in the time-averaged negative CRF, there is an increase in the time-averaged cloud albedo from 0.47 in the control run to 0.63 in the high-aerosol run. Increasing

aerosol concentrations and associated decreases in cloud-particle size as well as increases in the LWP and the IWP contribute to the increases in the negative CRF and cloud albedo. For example, the averaged effective radius of droplets over cloudy grid points with non-zero cloud-liquid mixing ratio and over the period decreases from 6.8 micron in the control run to 5.3 micron in the high-aerosol run.

It is well-known that updrafts or updraft mass fluxes control condensation by determining the level of supersaturation; in general, increasing updraft mass fluxes enhance condensation. Hence, to understand the increase in condensation and associated increases in LWP that affect aerosol-induced changes in the precipitation amount, CRF and cloud albedo, in the following Sect. 4.3, we investigate updraft mass fluxes and associated convergence.

4.3 Dynamics

4.3.1 Updrafts

The vertical distributions of the time- and area-averaged updraft mass fluxes are shown in Fig. 6. Larger updraft mass fluxes develop in the high-aerosol run than in the control run. The largest updraft mass flux and the largest differences in updraft mass fluxes between the runs are found in a layer between 3 and 5 km. The vertical distributions of the time- and area-averaged condensation rates are depicted in Fig. 7. Associated with the largest updraft mass flux and the largest difference in updraft mass fluxes between the

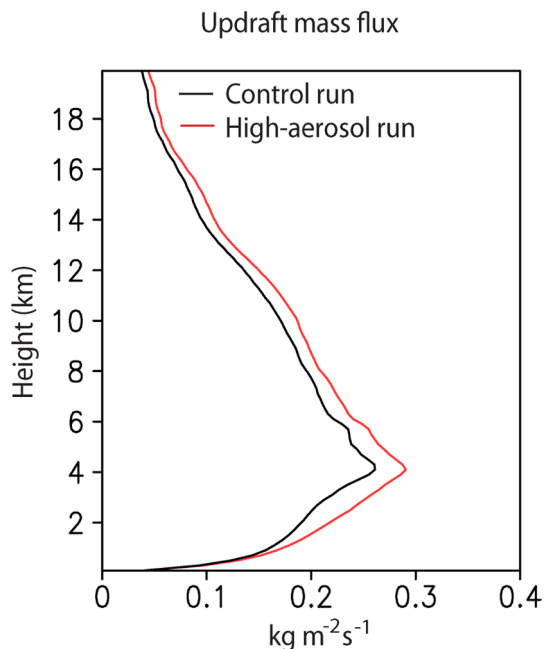


Fig. 6 Vertical distributions of the time- and area-averaged updraft mass fluxes for the control run and the high-aerosol run

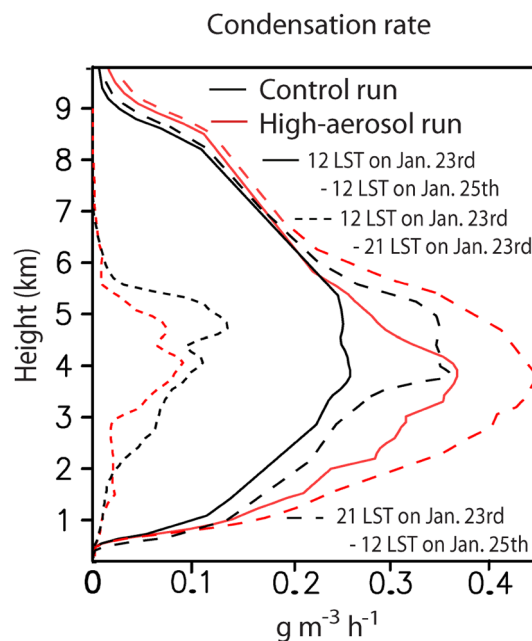


Fig. 7 Vertical distributions of the time- and area-averaged condensation rates for the control run and the high-aerosol run over different periods. *Solid lines* are for the period between 12:00 LST on January 23rd and 12:00 LST on January 25th. *Short-dashed lines* are for the period between 12:00 and 21:00 LST on January 23rd. *Long-dashed lines* are for the period between 21:00 LST on January 23rd and 12:00 LST on January 25th

runs in that layer, condensation rates and their difference between the runs are also largest in that layer.

Despite the larger initial stability and smaller convective available potential energy (CAPE), updrafts are stronger in the high-aerosol run than in the control run. The area-averaged CAPE is 2830 and 2310 J kg⁻¹ for the control run and the high-aerosol run, respectively, at 12:00 LST on January 23rd just before clouds start to form. If we consider the stability and CAPE only, it is expected that updrafts should be less intense in the high-aerosol run than in the control run, which is contrary to the results shown here.

The evolution of differences in the domain-averaged updraft mass fluxes between the control run and the high-aerosol run is shown in Fig. 8a. When cloud development is at its beginning stage, the larger stability suppresses updrafts more in the high-aerosol run than in the control run. However, around 21:00 LST on January 23rd, the sign of the difference in updrafts between the runs is reversed. Associated with this, as seen in Fig. 7, before 21:00 LST on January 23rd, condensation is larger in the control run, while after 21:00 LST on January 23rd, condensation is larger in the high-aerosol run. Solid lines in Fig. 9 show the frequency distributions of the updraft speed for the high-aerosol run and the control run over the period between 12:00 and 21:00 LST on January 23rd, which is the period

Fig. 8 Time series of differences in the area-averaged convergence at the surface, the domain-averaged updraft mass fluxes, negative buoyancy that is associated with evaporative cooling and downdraft mass fluxes **a** between the high-aerosol run and the control run and **b** between the high-aerosol-noevp run and the control-noevp run

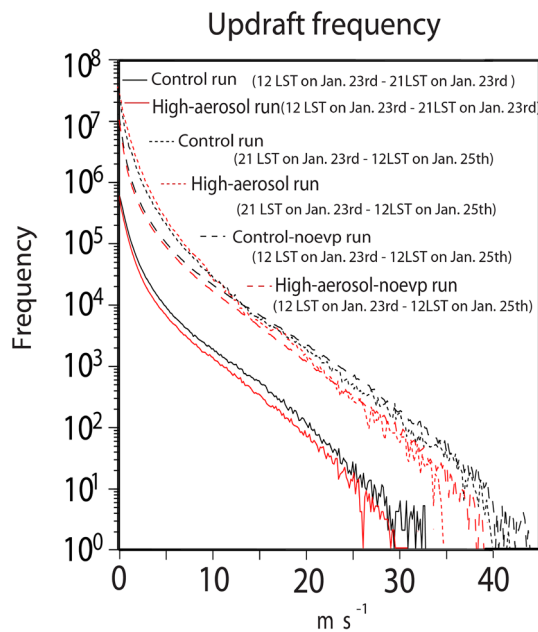
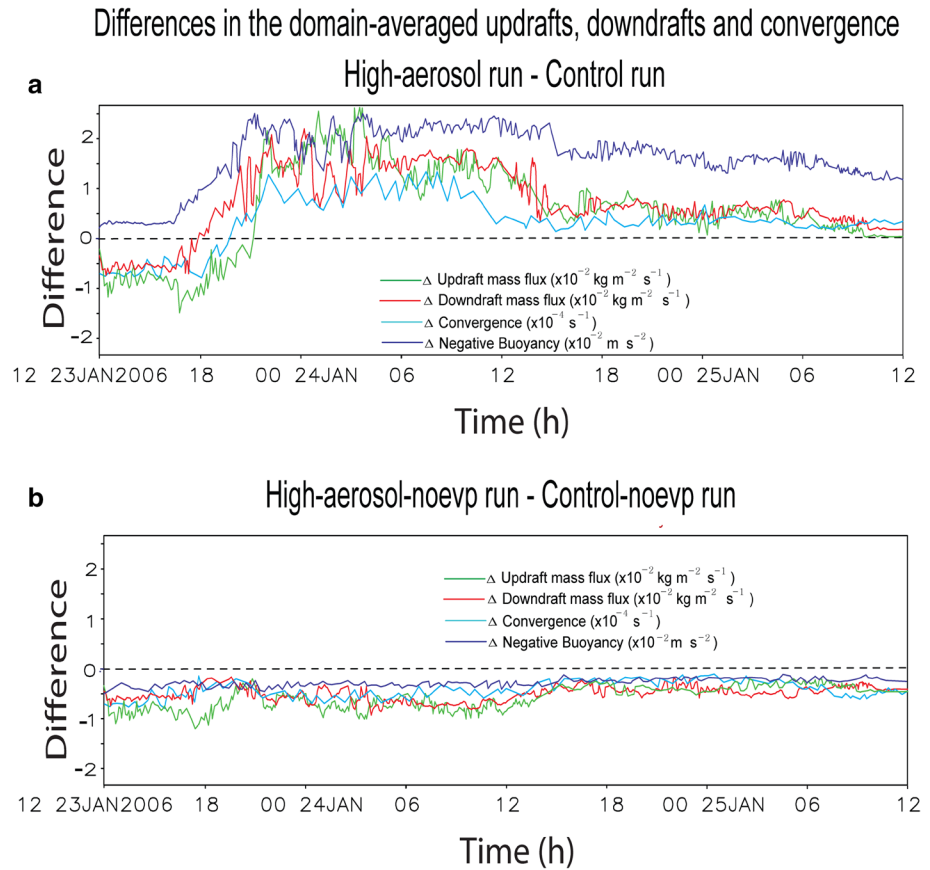


Fig. 9 Distributions of updraft frequency between 12:00 LST on January 23rd and 21:00 LST on January 23rd and between 12:00 LST on January 23rd and 12:00 LST on January 25th (short-dashed lines) in the control run and the high-aerosol run. Distributions for the period between 12:00 LST on January 23rd and 12:00 LST on January 25th (long-dashed lines) in the control-noevp run and the high-aerosol-noevp run are also shown

before the reversal in the sign of the difference in updrafts. Over all of the speed range, updrafts are less frequent in the high-aerosol run than in the control run, which results in the smaller domain-averaged updraft mass fluxes before 21:00 LST on January 23rd (Fig. 8a). However, the short-dashed lines in Fig. 9 shows that the frequency becomes larger for speeds below $\sim 10 \text{ m s}^{-1}$ while the frequency for speeds above $\sim 10 \text{ m s}^{-1}$ is still smaller in the high-aerosol run after 21:00 LST on January 23rd when the sign is reversed. Due to this, the sum of updraft speed over grid points with speeds below 10 m s^{-1} increases, while the sum of updraft speed above 10 m s^{-1} decreases with increasing aerosol concentrations between the control run and the high-aerosol run after 21:00 LST on January 23rd. The increases in the sum associated with updraft speed below 10 m s^{-1} are greater than the decreases in the sum associated with updraft speed above 10 m s^{-1} . This results in the larger domain-averaged updraft speed or updraft mass fluxes for all range of the updraft speed above 0 m s^{-1} in the high-aerosol run after 21:00 LST on January 23rd (Fig. 8a).

Updrafts are rooted in convergence around the surface. As the basic principle of cloud dynamics indicates, air that converges around the surface induces upward motion (or updrafts) to satisfy mass conservation. More intense convergence of air induces stronger updrafts. To examine the

root cause of the different evolutions of updrafts and condensation for the high-aerosol run and the control run, convergence fields at the surface are examined in the following Sect. 4.3.2.

4.3.2 Convergence

The convergence in this study is defined to be the absolute value of “ $\partial u/\partial x + \partial v/\partial y$ ” that has negative values. Here, u (v) are the horizontal wind in the x (y) direction. For the calculation of the area-averaged convergence, at each time step, we collect grid points with the negative values of “ $\partial u/\partial x + \partial v/\partial y$ ” by excluding grid points with its positive values (or by excluding divergence) at an altitude of interest. Then, we sum up those negative values over those grid points at the altitude. We take the absolute value of this sum that is divided by the number of all grid points (whether these grid points have negative values or not) over the horizontal domain and this absolute value is the area-averaged convergence at the altitude and each time step.

Convergence fields at the surface are superimposed on the column-averaged condensation rates as shown in Fig. 10. Here, for the column-averaged condensation rates, condensation rates at grid points where the updraft speed is lower than 10 m s^{-1} are collected for each grid column and the collected rates are summed over these grid points. This sum is divided by the number of all grid points in each grid column to obtain the column-averaged condensation rates. Figure 10a, b show the condensation and convergence fields at 18:00 LST on January 23rd when the domain-averaged updraft mass fluxes in the control run are greater (Fig. 8a). The control run shows the larger area-averaged convergence at the surface than the high-aerosol run does at 18:00 LST on January 23rd (Figs. 8a, 10a, b). Hence, the larger area-averaged surface convergence is correlated with the stronger updrafts that are averaged over the domain in the control run than in the high-aerosol run.

Remember that the large-scale forcings are identical among all of simulations in this study. Thus, there are no differences in convergence that is induced by large-scale forcings between the simulations in this study. This indicates that the differences in convergence are induced by different processes and associated motions at cloud scales between the simulations as detailed below.

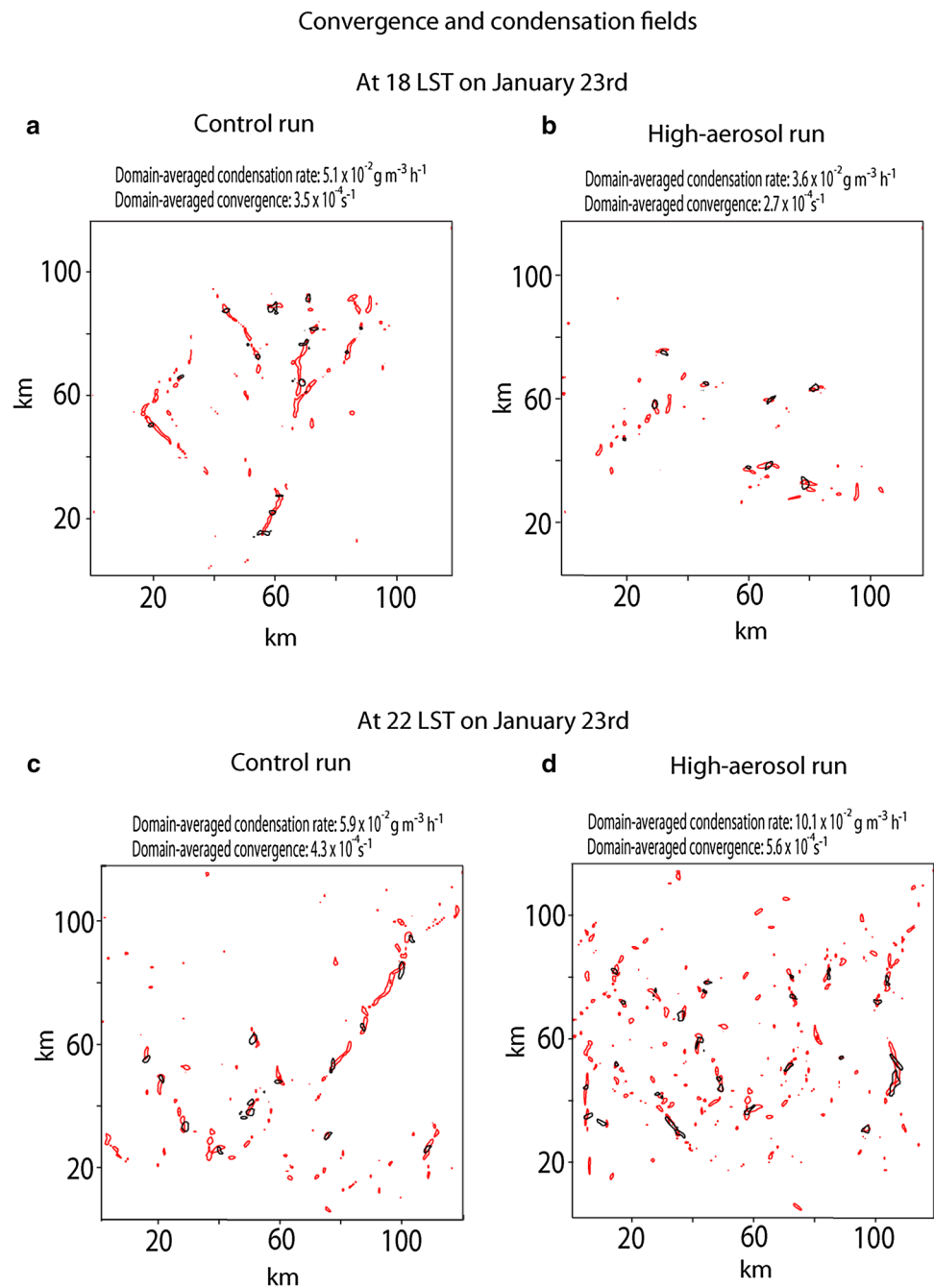
The greater domain-averaged updraft mass fluxes are due to the larger frequency of updrafts over the whole speed range in the control run before 21:00 LST on January 23rd (Fig. 9). More frequent updrafts induce more condensation entities, or cloud cells, in the control run than in the high-aerosol run as seen in Fig. 10a, b. More condensation entities produce a larger condensation rate that is averaged over the domain in the control run, despite the fact that individual condensation rates are similar between the

runs at 18:00 LST on January 23rd. This explains the larger domain-averaged condensation in the control run before 21:00 LST on January 23rd as shown in Fig. 7.

Figure 8a shows that the area-averaged surface convergence becomes larger at 19:30 LST on January 23rd, which eventually induces the larger domain-averaged updraft mass fluxes at 21:00 LST on January 23rd in the high-aerosol run. Figure 10c, d show the convergence and condensation fields at 22:00 LST on January 23rd, which is 1 h after the high-aerosol run starts to have greater updraft mass fluxes. As exemplified by Fig. 10c, d, the high-aerosol run shows the greater area-averaged surface convergence, which provides favorable conditions for the development of more numerous updrafts with speeds under 10 m s^{-1} after 21:00 LST on January 23rd as shown in Fig. 9. The more frequent occurrence of updrafts with speeds under 10 m s^{-1} in turn provides favorable conditions for the development of more numerous condensation entities that can be considered to be cloud cells, in the high-aerosol run than in the control run after 21:00 LST on January 23rd (Fig. 10c, d). More condensation entities lead to the greater domain-averaged condensation rate in the high-aerosol run after 21:00 LST on January 23rd (Fig. 7), although individual condensation rates are similar between the runs. Note that as shown in Fig. 9, for updrafts with speeds above 10 m s^{-1} , there is a smaller frequency of updrafts after 21:00 LST on January 23rd in the high-aerosol run, which is associated with the smaller number of condensation entities and the smaller averaged condensation rate in the high-aerosol run after 21:00 LST on January 23rd when it comes to updrafts with speeds above 10 m s^{-1} and condensation produced by them. This smaller averaged condensation rate associated with updrafts having speeds above 10 m s^{-1} is offset by the larger averaged condensation rate associated with updrafts having speeds under 10 m s^{-1} . This offset results in the greater domain-averaged condensation rate in the high-aerosol run than in the control run. To obtain the averaged condensation rate associated with the updraft speed above (below) 10 m s^{-1} , we collect condensation rates over grid points with updrafts whose speeds are above (below) 10 m s^{-1} and sum those rates over these grid points. This sum is divided by the number of all grid points over the whole domain whether these grid points have the updraft speed above 10 m s^{-1} or below 10 m s^{-1} or 0 m s^{-1} and this sum divided is the averaged condensation rate associated with the updraft speed above (below) 10 m s^{-1} .

Aerosol-induced increases in evaporation strengthen cold pool by cooling the atmosphere more. Here, cold pool is composed of downdrafts where evaporation and associated cooling occur (Houze 1993). Associated with the strengthened cold pool that provides enhanced negative buoyancy, there are increases in the intensity of downdrafts or air parcels that move downward. These

Fig. 10 Superposition of vertically averaged rates of condensation collocated with updrafts lower than 10 m s^{-1} , represented by black contours for $1.5 \text{ g m}^{-3} \text{ h}^{-1}$, and the convergence field at the surface, represented by red contours for $1.7 \times 10^{-2} \text{ s}^{-1}$. **a** and **c** are for the control run, **b** and **d** are for the high-aerosol run. **a** and **b** are for 18:00 LST on January 23rd, **c** and **d** are for 22:00 LST on January 23rd



downdrafts with their enhanced intensity reach the surface and generate a stronger outflow that spreads to the environment. The stronger outflow collides with warm air in the environment to form more intense convergence and updrafts (Lee et al. 2010; Storer et al. 2010; Lee 2011b). In particular, aerosol-induced increases in cloud-liquid evaporation are closely linked to the enhancement of the intensity of downdrafts (Lee et al. 2008a, b, 2010; Lee 2011b). Cloud liquid or droplets in downdrafts move together with downdrafts, thus, when downdrafts

descend, cloud liquid descends while being included in downdrafts. Cloud liquid in the descending downdrafts evaporates. More evaporation of cloud liquid provides greater negative buoyancy to downdrafts so that they accelerate or intensify more (Byers and Braham 1949; Grecni and Nese 2001). Motivated by this, in the following Sect. 4.3.3, we examine downdrafts and associated cloud-liquid evaporation as a way of better understanding aerosol-induced changes in convergence.

4.3.3 Evaporation and downdrafts

The vertical distribution of the time- and area-averaged evaporation rate over the period between 12:00 and 21:00 LST on January 23rd when updraft mass fluxes start to be greater in the high-aerosol run than in the control run is depicted in Fig. 11. Figure 11 shows that there is larger (smaller) cloud-liquid (rain) evaporation in the high-aerosol run. Most of evaporation above ~ 2 km is due to cloud-liquid evaporation, while most of evaporation below ~ 2 km is due to rain evaporation. Less autoconversion induces the larger (smaller) cloud-liquid (rain) evaporation in the high-aerosol run than in the control run by enhancing (reducing) the amount of available cloud liquid (rain) for evaporation. Due to more cloud-liquid evaporation, there is larger evaporation-related negative buoyancy and this eventually develops stronger downdrafts at 18:00 LST on January 23rd (Fig. 8a).

It is notable that when the stronger outflow driven by stronger downdrafts collides with warm air, there is the formation of more extensive convergence around the surface as shown in Fig. 10c, d and simulated by Lee et al. (2008a, b) and Lee (2011b). In other words, the areal extent of convergence or the number of grid points at which convergence occurs becomes larger with increasing aerosol

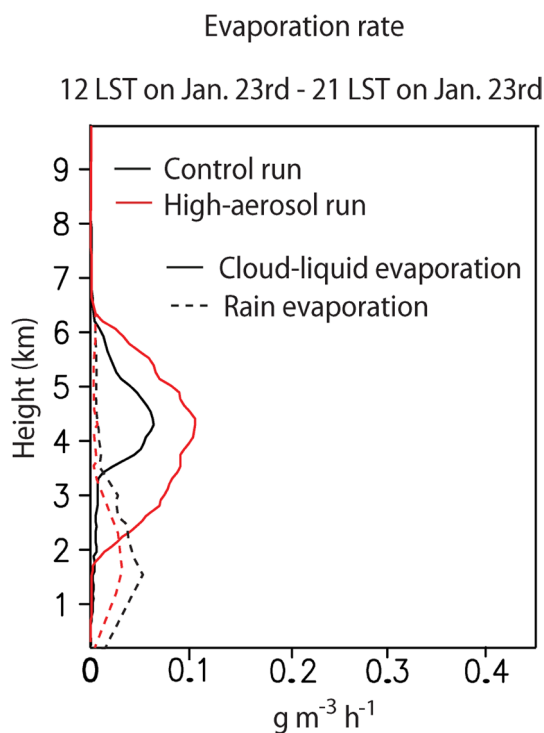


Fig. 11 Vertical distributions of the time- and area-averaged cloud-liquid and rain evaporation rates over the period between 12:00 and 21:00 LST on January 23rd for the control run and the high-aerosol run

concentrations, which triggers convergence that is averaged over the domain and greater in the high-aerosol run than in the control run. Associated with this, air parcels are more numerous in the convergence field in the high-aerosol run. This induces more air parcels to move up and thus generates more updraft cores in the high-aerosol run than in the control run. More updraft cores induce more competition among them for heat and moisture in the high-aerosol run. Thus, lower convective energy is assigned to some of individual cores in the high-aerosol run compared to the situation with less competition, which was also simulated by Lee et al. (2008b) and Lee (2011b). This reduces the updraft speeds of those individual cores with the smaller amount of energy, which turns a portion of those updraft cores that have speeds greater than 10 m s^{-1} and those updraft cores that can potentially grow to have speeds greater than 10 m s^{-1} to updraft cores that have speeds lower than 10 m s^{-1} in the high-aerosol run. This in turn triggers a larger frequency of updrafts with speeds lower than 10 m s^{-1} and a smaller frequency of updrafts with speeds greater than 10 m s^{-1} in the high-aerosol run than in the control run after 21:00 LST on January 23rd.

For further examination of the roles played by increases in cloud-liquid evaporation with increasing aerosol concentrations in the stronger downdrafts, the high-aerosol run and the control run are repeated with cooling from cloud-liquid evaporation turned off and cooling from rain evaporation left on. The repeated runs are named the high-aerosol-noevp run and the control-noevp run, respectively. In these runs, cloud-liquid mass reduces due to cloud-liquid evaporation, although cloud-liquid evaporation does not affect temperature via its latent-heat absorption. As shown in Fig. 8b, negative buoyancy from rain evaporation and downdrafts are weaker in the high-aerosol-noevp run than in the control-noevp run throughout the whole simulation period. Due to this, convergence and updrafts are also less intense in the high-aerosol-noevp run throughout the whole simulation period. Associated with this, the long-dashed lines in Fig. 9 depict that the frequency of updrafts is smaller in the high-aerosol-noevp run than in the control-noevp run over all of the speed range. This demonstrates that the enhanced cloud-liquid evaporation and intensity of convergence that are induced by increasing aerosol concentrations are the main causes of the greater domain-averaged updraft mass fluxes and condensation.

Here, we see that the response of updrafts to increasing aerosol concentrations is selective, which is that while the frequency of some portions of updrafts increases, that of other portions of updrafts reduces with increasing aerosol concentrations. Different types of updrafts control different cloud types with different depths, considering that in general, strong (weak) updrafts generate and maintain deep (shallow) clouds. Hence, this selective response of updrafts

is likely to induce the selective response of clouds. Stated differently, due to the selective response of updrafts, it is likely that there are different responses of clouds among clouds with different depths, which alter cloud-depth spatiotemporal distributions or cloud-system organization. Motivated by this and the fact that studies of the effects of BC aerosol on clouds in the context of cloud-system organization have been rare, in the following Sect. 4.4, we examine this aspect of aerosol effects on cloud-system properties (i.e., cloud-system organization) and associated changes in precipitation properties.

4.4 Cloud-depth and precipitation distributions

Figure 12 shows the frequency distribution of precipitation rates collected over all of the time steps and at all of the grid points at the surface. While a large difference in

cumulative precipitation between the high-aerosol run and the control run is not seen, the frequency distributions of precipitation rate between the two runs have different features (Fig. 12a, b). For precipitation rates lower than $\sim 7.5 \text{ mm h}^{-1}$, the high-aerosol run shows the higher frequency than the control run does. The reverse is true for precipitation rates greater than $\sim 7.5 \text{ mm h}^{-1}$ (Fig. 12a, b). Hence, we can see that the increases in aerosol concentration and absorption of solar radiation by aerosols enhance relatively light precipitation, while suppressing relatively heavy precipitation. The precipitation, which is suppressed and has rates higher than $\sim 7.5 \text{ mm h}^{-1}$, is compensated by the precipitation that is enhanced and has rates lower than $\sim 7.5 \text{ mm h}^{-1}$ in the high-aerosol run. This results in the small difference in cumulative precipitation.

Figure 13 shows the frequency distributions of cloud depths, which represent cloud-depth spatiotemporal distributions. These cloud depths are collected over all of the time steps and in all of the cloud cells. The frequency of clouds having depths greater than $\sim 5 \text{ km}$ is smaller in the high-aerosol run, while the frequency of clouds having depths smaller than $\sim 5 \text{ km}$ is higher in the high-aerosol run (Fig. 13).

As seen in Fig. 14 for the control run, precipitation rates and cloud depths are proportional. In general, clouds with depths greater than $\sim 5 \text{ km}$ produce precipitation rates greater than $\sim 7.5 \text{ mm h}^{-1}$. Clouds whose depths are lower than $\sim 5 \text{ km}$ produce precipitation rates lower than $\sim 7.5 \text{ mm h}^{-1}$. Concerning Fig. 14, a precipitation rate at the bottom of each cloudy column together with the vertical extent,

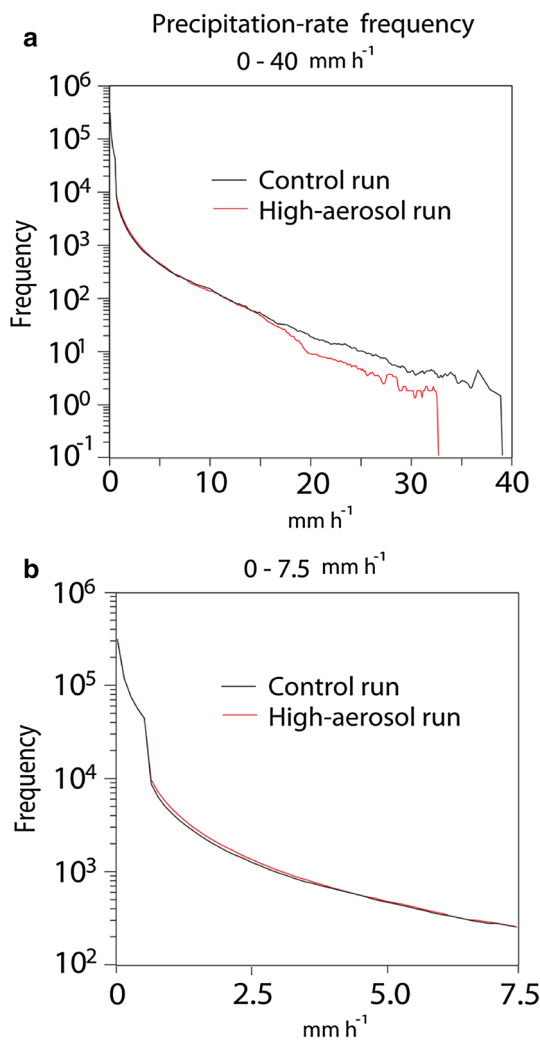


Fig. 12 Distributions of precipitation-rate frequency **a** for rates between 0 and 40 mm h^{-1} and **b** for rates between 0 and 7.5 mm h^{-1} in the control run and the high-aerosol run

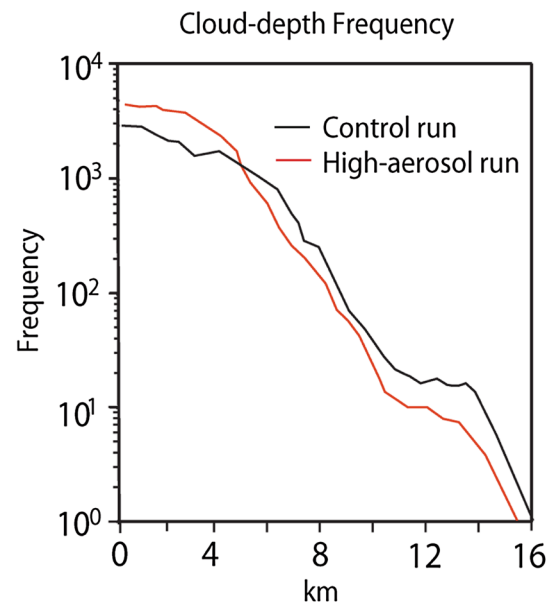
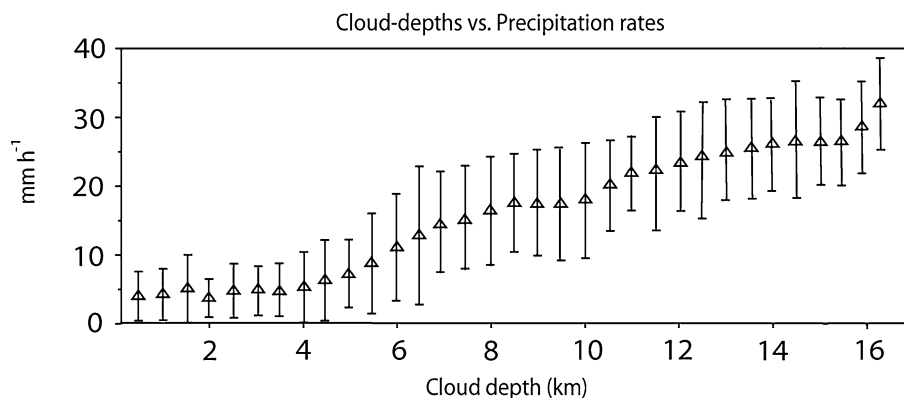


Fig. 13 Distributions of cloud-depth frequency for the control run and the high-aerosol run

Fig. 14 Precipitation rates as a function of cloud depth for the control run. One standard deviation of precipitation rate is shown by vertical bars

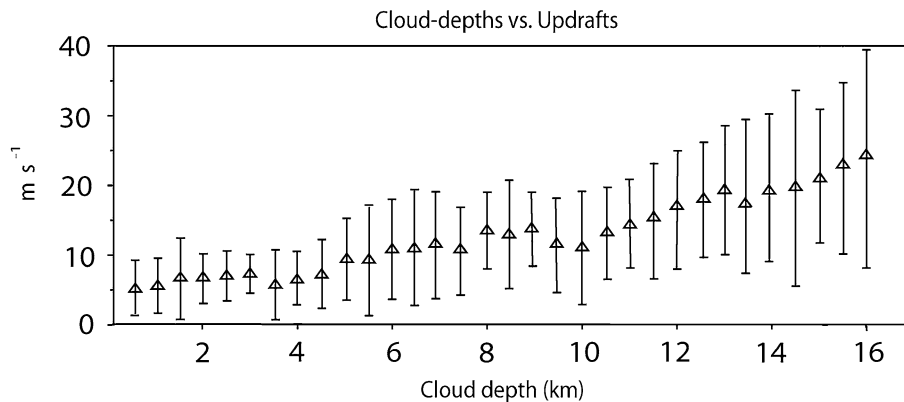


or depth, of a cloud layer whose bottom is located closest to the surface in each of those columns is obtained at each time step. Then, precipitation rates collected over those columns and all time steps are classified by the depths and the average and standard deviation of precipitation rates for each of the depths are calculated. Differences in the precipitation-rate distribution (or the average and standard deviation of precipitation rates) between the control run and the high-aerosol run for each cloud depth are smaller than 10% (not shown), although the control-run cloud depth reaches ~ 16 km and the high-aerosol-run depth reaches ~ 15 km (Fig. 13). In other words, for the high-aerosol run, we can also say that clouds with depths greater than ~ 5 km produce precipitation rates greater than ~ 7.5 mm h⁻¹ and clouds whose depths are lower than ~ 5 km produce precipitation rates lower than ~ 7.5 mm h⁻¹. We have also obtained all updrafts at grid points where clouds exist in each of cloudy columns together with the vertical extent, or depths, of cloud layers in each of those columns at each time step. Those updrafts are then classified by the depths and the average and standard deviation of those updrafts for each of the depths are calculated. By doing this, we are able to obtain the relation between cloud depth and updrafts for the control run (Fig. 15). In general, updrafts with speeds lower (higher) than ~ 10 m s⁻¹ are generally linked to clouds

with depths smaller (greater) than 5 km. This is also applicable to the high-aerosol run, because similar to Fig. 14, differences in the updraft distribution (or the average and standard deviation of updrafts) between the runs for each of the cloud depths are smaller than 10%. The relationship among cloud depths, precipitation rates, and updrafts in Figs. 14 and 15 is applicable to both the high-aerosol run and the control run, thus, it can be said that associated with the more intense convergence and more numerous updrafts below 10 m s⁻¹ as shown in Sect. 4.3, there is a larger number of clouds whose depths are lower than ~ 5 km in the high-aerosol run and this induces the high-aerosol run to have the larger frequency of precipitation with rates below ~ 7.5 mm h⁻¹ than that in the control run. Less numerous updrafts with speeds above 10 m s⁻¹ are associated with a smaller number of clouds with depths greater than ~ 5 km in the high-aerosol run. This induces the high-aerosol run to have the smaller frequency of precipitation rates above ~ 7.5 mm h⁻¹ than that in the control run.

BC aerosol affects surface heat fluxes by modulating solar radiation that reaches the surface. Surface heat fluxes in turn affect the development of convection or updrafts, hence, aerosol-induced changing surface heat fluxes can play a role in above-described changing updrafts and thus clouds and precipitation with increasing

Fig. 15 Updrafts as a function of cloud depth for the control run. One standard deviation of updrafts is shown by vertical bars



aerosol concentrations. In the following Sect. 4.5, this role is examined.

4.5 Surface heat fluxes

Figure 16a, b show scatterplots of surface heat flux (latent plus sensible heat fluxes in W m^{-2}) as a function of precipitation rate in the control run and the high-aerosol run, respectively. For precipitation rates lower than 7.5 mm h^{-1} , the high-aerosol run shows more data points than the control run does, consistent with Fig. 12a, b, which shows that the high-aerosol run has more frequent precipitation with rates lower than 7.5 mm h^{-1} . These more frequent occurrences of precipitation rates lower than 7.5 mm h^{-1} are associated with the fact that the high-aerosol run shows more frequent occurrences of surface heat fluxes below $\sim 200 \text{ W m}^{-2}$ (Fig. 16). However, for precipitation that has rates above 7.5 mm h^{-1} , the control run shows more data points. These data points are associated with surface heat fluxes greater than $\sim 200 \text{ W m}^{-2}$.

Concerning the high-aerosol run (control run), more points representing surface heat fluxes lower (greater) than $\sim 200 \text{ W m}^{-2}$ are associated with more numerous clouds whose depths are lower (higher) than $\sim 5 \text{ km}$, which in turn produce more light (heavy) precipitation

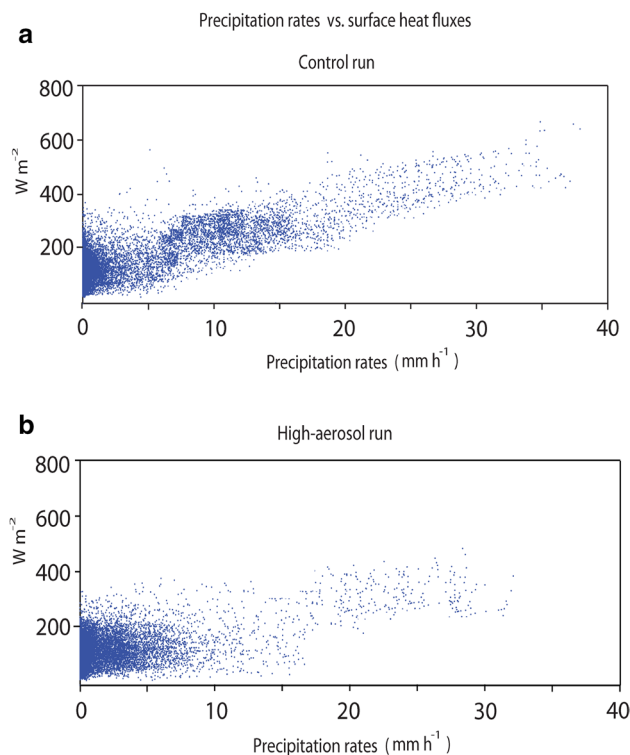


Fig. 16 Scatterplots of the joint distributions of precipitation rates and surface heat fluxes (latent plus sensible heat fluxes) for **a** the control run and **b** the high-aerosol run

whose rates are below (above) $\sim 7.5 \text{ mm h}^{-1}$ (Figs. 12, 13, 14, 16). Due to the larger concentration of aerosols that absorb solar radiation in the high-aerosol run, the high-aerosol run has the smaller solar radiation reaching the surface than the control run does. Associated with this, in the high-aerosol run, there are more (less) occurrences of the low (high) surface heat fluxes lower (greater) than $\sim 200 \text{ W m}^{-2}$. This situation with surface fluxes works in tandem with aerosol-induced increases in the intensity of convergence to produce more occurrences of precipitation whose rates are below $\sim 7.5 \text{ mm h}^{-1}$ and less occurrences of precipitation whose rates are above $\sim 7.5 \text{ mm h}^{-1}$ in the high-aerosol run than in the control run.

5 Summary and discussion

5.1 Summary

This study examined the effects of interplay between aerosol absorption, thermodynamics, dynamics, and microphysics on clouds and precipitation in the context of cloud-system organization and precipitation distributions.

Despite the increases in stability or the decreases in CAPE with increases in the concentration of absorbing aerosols, $\sim 9 \text{ h}$ after clouds start to form, decreases in the averaged updraft mass fluxes (which are induced by the increases in stability) turn into their increases that are maintained to the end of the simulations. This is mainly due to aerosol-induced increases in cooling from cloud-liquid evaporation, which intensifies downdrafts and convergence. The intensified convergence selectively enhances the frequency of weak updrafts with speeds lower than $\sim 10 \text{ m s}^{-1}$, which is supported by increases in the occurrence of low surface heat fluxes with values lower than $\sim 200 \text{ W m}^{-2}$ and results in the increases in the averaged updraft mass fluxes. The increase in the frequency of weak updrafts with speeds lower than $\sim 10 \text{ m s}^{-1}$ supports the development of more shallow clouds whose depths are lower than $\sim 5 \text{ km}$. These more shallow clouds produce more weak precipitation whose rates are lower than $\sim 7.5 \text{ mm h}^{-1}$. The increases in the weak-updraft frequency for the updraft speed lower than $\sim 10 \text{ m s}^{-1}$ enable condensation to increase and this in turn enables increases in the LWP and the accretion of cloud liquid by precipitation. These increases in accretion offset suppressed autoconversion and thus result in the negligible variation in cumulative precipitation with varying aerosol concentrations. The increases in the LWP contribute to the 63% increase in the negative CRF and the 23% increase in cloud albedo.

5.2 Discussion

5.2.1 Aerosol effects on CAPE and horizontal temperature gradient

When there is local evaporative cooling, as in this study, an air column with a low temperature is generated. This air column with the low temperature corresponds to cold pool. This air column creates a horizontal temperature gradient by making temperature contrast with an air column having surrounding warm air with a high temperature. The greater evaporative cooling creates greater temperature contrast or a greater horizontal temperature gradient between the columns. Generating this greater temperature contrast, aerosol-induced greater evaporative cooling results in the more intense development of downdrafts, convergence, and updrafts as simulated in this study.

The traditional understanding of BC-aerosol effects on clouds in the previous studies indicates that aerosol-induced increases in radiative heating can make cold air above warm air less cold and thus make the vertical temperature gradient and CAPE smaller, which in turn potentially makes the warm air below rise up with weaker updrafts (Feingold et al. 2005; Ramana et al. 2010; Jacobson 2012). This study indicates that this traditional understanding based on CAPE and the associated vertical temperature gradient does not give us a full picture of how BC aerosols affect cloud systems. This study demonstrates that to obtain a full picture from the results presented here, we need to pay our attention to the horizontal temperature gradient.

5.2.2 Comprehensive approaches to aerosol effects

This study demonstrates that it is not wise to consider only stability (based on CAPE regarding the vertical temperature gradient) and domain-averaged cloud properties (e.g., the domain-averaged cumulative precipitation) as a way of identifying the signature of BC-aerosol effects on clouds as is done in the traditional approach. This study shows that the response of updraft, cloud-depth, and precipitation-rate frequencies to the effect of aerosol perturbations on the horizontal temperature gradient bears a strong signature of BC-aerosol effects. Hence, for more comprehensive studies of aerosol-cloud interactions, we should look into more diverse aspects of these interactions by incorporating more thermodynamic variables such as the horizontal temperature gradient (in addition to CAPE or associated vertical temperature gradient), cloud-system properties (e.g., the frequency of cloud-cell depths), cloud microphysical and dynamic processes (e.g., evaporation and updraft frequency), and more precipitation properties such as precipitation-rate frequency (in addition to the precipitation amount). For the comprehensive future studies, the

geostationary satellite and radar can be useful, considering that they are able to identify cloud-system and precipitation properties with high-level time and spatial resolutions.

Acknowledgements This study is supported by the National Science Foundation (NSF) (grants AGS1118325 and AGS1534670), the National Oceanic and Atmospheric Administration (NOAA) (grant NOAA-NWS-NWSP0-2015-2004117), Korea Environmental Industry and Technology Institute funded by the Korea Ministry of Environment as “Climate Change Correspondence Program”, and NIER2016-29: Extension of GEMS Product.

References

- Allen G, Vaughan G, Bower KN et al (2008) Aerosol and trace-gas measurement in the Darwin area during the wet season. *J Geophys Res* 113:D06306, doi:[10.1029/2007JD008706](https://doi.org/10.1029/2007JD008706)
- Andreae MO et al (2004) Smoking rain clouds over the amazon. *Science* 303:1337–1341
- Baker MB, Charlson RJ (1990) Bistability of CCN concentrations and thermodynamics in the cloud-topped boundary layer. *Nature* 345:142–145
- Byers HR, Braham RR (1949) The thunderstorms. U.S. Govt. Printing Office, Washington, p 287
- Chen F, Dudhia J (2001) Coupling an advanced land-surface hydrology model with the Penn State-NCAR MM5 modeling system. Part I: Model description and implementation. *Mon Wea Rev* 129:569–585
- Feingold G, Kreidenweis SM (2002) Cloud processing of aerosol as modeled by a large eddy simulation with coupled microphysics and aqueous chemistry. *J Geophys Res* 107:4687. doi:[10.1029/2002JD002054](https://doi.org/10.1029/2002JD002054)
- Feingold G, Jiang H, Harrington JY (2005) On smoke suppression of clouds in Amazonia. *Geophys Res Lett* 32:L02804. doi:[10.1029/2004GL021369](https://doi.org/10.1029/2004GL021369)
- Fouquart Y, Bonnel B (1980) Computations of solar heating of the Earth's atmosphere: a new parameterization. *Beitr Phys Atmos* 53:35–62
- Fridlind A et al (2010) ARM/GCSS/SPARC TWP-ICE CRM inter-comparison study, available at <http://pubs.giss.nasa.gov/abs/fr08100v.html>
- Fridlind AM et al (2012) A comparison of TWP-ICE observational data with cloud-resolving model results. *J Geophys Res* 117:D05204. doi:[10.1029/2011JD016595](https://doi.org/10.1029/2011JD016595)
- Grenci LM, Nese JM (2001) A world of weather: fundamentals of meteorology: a text/ laboratory manual, Kendall/Hunt Publishing Company, USA
- Heylighen F (2002) The science of self-organization and adaptivity, knowledge management, organizational intelligence and learning and complexity (ed. Kiel LD) in encyclopedia of life support systems 1–26, available via <http://www.eolss.net>, Eolss Publishers, Oxford
- Houze RA (1993) Cloud dynamics, Academic Press, London, p 573
- Jacobson MZ (2006) Effects of externally-through-internally-mixed soot inclusions within clouds and precipitation on global climate. *J Phys Chem A* 110:6860–6873
- Jacobson MZ (2012) Investigating cloud absorption effects: Global absorption properties of black carbon, tar balls, and soil dust in clouds and aerosols. *J Geophys Res* 117:D06205. doi:[10.1029/2011JD017218](https://doi.org/10.1029/2011JD017218)
- Lau WK-M, Ramanathan V, Wu G-X, Li Z, Tray SC, Hsu C, Sikka R, Holben B, Lu D, Tartari G, Chin M, Koudelova P, Chen H, Ma Y, Huang J, Taniguchi K, Zhang R (2008) The joint

- aerosol–monsoon experiment: a new challenge for monsoon climate research. *Bull Amer Meteorol Soc* 89:369–383
- Lee SS (2011a) Aerosols, clouds and climate. *Nat Geosci* 4:826–827
- Lee SS (2011b) Dependence of aerosol-precipitation interactions on humidity in a multiple-cloud system. *Atmos Chem Phys* 11:2179–2196
- Lee SS, Feingold G (2013) Aerosol effects on the cloud-field properties of tropical convective clouds. *Atmos Chem Phys* 13:6713–6726
- Lee SS, Donner LJ, Phillips VTJ, Ming Y (2008a) The dependence of aerosol effects on clouds and precipitation on cloud-system organization, shear and stability. *J Geophys Res* 113:D16202. doi:[10.1029/2007JD009224](https://doi.org/10.1029/2007JD009224)
- Lee SS, Donner LJ, Phillips VTJ, Ming Y (2008b) Examination of aerosol effects on precipitation in deep convective clouds during the 1997 ARM summer experiment. *Q J R Meteorol Soc* 134:1201–1220. doi:[10.1002/qj.287](https://doi.org/10.1002/qj.287)
- Lee SS, Donner LJ, Penner JE (2010) Thunderstorm and stratocumulus: how does their contrasting morphology affect their interactions with aerosols?. *Atmos Chem. Phys* 10:6819–6837. doi:[10.5194/acp-10-6819-2010](https://doi.org/10.5194/acp-10-6819-2010)
- Lee SS, Feingold G, Koren I et al (2014a) Effect of gradients in biomass burning aerosol on circulations and clouds. *J Geophys Res* 119:9948–9964
- Lee SS, Tao W-K, Jung CH (2014b) Aerosol effects on instability, circulations, clouds and precipitation. *Adv Meteorol* 2014:683950
- Meyers MP, Walko RL, Harrington JY, Cotton WR (1997) New RAMS cloud microphysics parameterization. Part II. The two-moment scheme. *Atmos Res* 45:3–39
- Mlawer EJ, Taubman SJ, Brown PD, Iacono MJ, Clough SA (1997) RRTM, a validated correlated-k model for the longwave. *J Geophys Res* 102:16663–16682
- Morrison H, de Boer G, Feingold G et al (2012) Resilience of persistent Arctic mixed-phase clouds. *Nat Geosci* 5:11–17. doi:[10.1038/ngeo1332](https://doi.org/10.1038/ngeo1332)
- Qian Y, Gong D, Fan J, Leung LR, Bennartz R, Chen D, Wang W (2009) Heavy pollutions suppresses light rain in China: observations and modelling. *J Geophys Res* 114:D00K02. doi:[10.1029/2008JD011575](https://doi.org/10.1029/2008JD011575)
- Ramana MV, Ramanathan V, Feng Y, Yoon S-C, Kim S-W, Carmichael GR, Schauer JJ (2010) Warming influenced by the ratio of black carbon to sulphate and the black-carbon source. *Nat Geosci* 3:542–545
- Ramanathan V, Crutzen PJ, Lelieveld J, Mitra AP, Althausen D, erson J et al (2001) Indian ocean experiment: an integrated analysis of the climate forcing and effects of the great Indo-Asian haze. *J Geophys Res* 106:28371–28398
- Rosenfeld D (1999) TRMM observed first direct evidence of smoke from forest fires inhibiting rainfall. *Geophys Res Lett* 26:3105–3108
- Saleeby SM, Cotton WR (2004) A large-droplet mode and prognostic number concentration of cloud droplets in the Colorado state university regional atmospheric modeling system (RAMS). Part I: module description and supercell test simulations. *J Appl Meteor* 43:182–195
- Saleeby SM, Cotton WR (2008) A binned approach to cloud droplet riming implement in a bulk microphysics model. *J Appl Meteor Climatol* 47:694–703
- Segal M, Arritt RW (1992) Nonclassical mesoscale circulations caused by surface heat flux gradients. *Bull Amer Meteor Soc* 1593–1604
- Storer RL, van den Heever SC, Stephens GL (2010) Modeling aerosol impacts on convection under differing storm environments. *J Atmos Sci* 67:3904–3915
- Tao W-K, Chen J-P, Li Z, Wang C, Zhang C (2012) Impact of aerosols on convective clouds and precipitation. *Rev Geophys* 50:RG2001. doi:[10.1029/2011RG000369](https://doi.org/10.1029/2011RG000369)
- Ten Hoeve JE, Jacobson MZ, Remer LA (2012) Comparing results from a physical model with satellite and in situ observations to determine whether biomass burning aerosols over the Amazon brighten or burn off clouds. *J Geophys Res* 117:D08203. doi:[10.1029/2011JD016856](https://doi.org/10.1029/2011JD016856)
- Vaughan G et al (2008) SCOUT-O3/ACTIVE: High-altitude aircraft measurements around deep tropical convection. *Bull Amer Meteorol Soc* 89:647–662
- Walko RL, Cotton WR, Meyers MP, Harrington JY (1995) New RAMS cloud microphysics parameterization: Part I. The single-moment scheme. *Atmos Res* 38:29–62
- Wang C (2009) The sensitivity of tropical convective precipitation to the direct radiative forcings of black carbon aerosols emitted from major regions. *Ann Geophys* 27:3705–3711
- Wang C (2013) Impact of anthropogenic absorbing aerosols on clouds and precipitation: a review of recent progresses. *Atmos Res* 122:237–249
- Wang H, Skamarock WC, Feingold G (2009) Evaluation of scalar advection schemes in the Advanced Research WRF model using large-eddy simulations of aerosol-cloud interactions. *Mon Wea Rev* 137:2547–2558
- Zhu P et al (2012) A limited area model (LAM) intercomparison study of a TWP-ICE active monsoon mesoscale convective event. *J Geophys Res* 117:D11208. doi:[10.1029/2011JD016447](https://doi.org/10.1029/2011JD016447)